frontiers | Frontiers in Astronomy and Space Sciences

TYPE Original Research
PUBLISHED 02 October 2024
DOI 10.3389/fspas.2024.1472874

OPEN ACCESS

EDITED BY
Chen Shi,
University of California, Los Angeles,
United States

REVIEWED BY
Masaru Nakanotani,
University of Alabama in Huntsville,
United States
Xu Zhang,
University of California, Los Angeles,
United States

*CORRESPONDENCE
L. Zhao,
lzh@umich.edu

RECEIVED 30 July 2024
ACCEPTED 12 September 2024
PUBLISHED 02 October 2024

CITATION
Carpenter DT, Lepri ST, Zhao L, Dewey RM, Raines JM, Livi S, Galvin AB and Kistler LM (2024) The solar wind heavy ion composition in the ascending phases of the solar cycles 23 and 25.
Front. Astron. Space Sci. 11:1472874.
doi: 10.3389/fspas.2024.1472874

The solar wind heavy ion composition in the ascending phases of the solar cycles 23 and 25

D. T. Carpenter[1], S. T. Lepri[1], L. Zhao[1]*, R. M. Dewey[1], J. M. Raines[1], S. Livi[1,2], A. B. Galvin[3] and L. M. Kistler[3]

[1]Climate and Space Sciences and Engineering, University of Michigan, Ann Arbor, MI, United States, [2]Space Science and Engineering, Southwest Research Institute, San Antonio, TX, United States, [3]Physics and Astronomy, University of New Hampshire, Durham, NH, United States

The approximately 11-year solar cycle has been shown to impact the heavy ion composition of the solar wind, even when accounting for streams of differing speeds; however, the heavy ion composition observed between the same specific phases of a past solar cycle and the current cycle has rarely, if ever, been compared. Here, we compare the heavy ion composition of the solar wind, as measured *in situ* during the solar cycle 23 and 25 ascending phases. We examine the mean iron and oxygen charge state composition and the O^{7+}/O^{6+} ratio in multiple ranges of associated bulk wind speeds. Then, we compare the iron and oxygen charge state composition and relative abundance of iron to oxygen in the traditionally defined fast and slow solar wind. Finally, to determine the impact of individual ion contributions on the solar wind iron abundance, we examine individual ratios of iron and oxygen ions. Although the charge state composition remained broadly similar between these two ascending phases, both the O^{7+}/O^{6+} ratio and iron fractionation in fast-speed streams were higher in the solar cycle 25 ascending phase than they were during the solar cycle 23 ascending phase, suggesting that equatorial coronal hole fields more frequently reconnected with helmet streamers or active regions in the latter of the two ascending phases; however, more work will need to be done to connect these observations back to their coronal origins. The individual ion ratios used in this work provided a spectrum to analyze the aggregate elemental abundances, and this work, as a whole, is an important step in determining how conditions in the corona may vary between solar cycles between the same phases.

KEYWORDS

Sun, solar wind, composition, charge state, solar cycle, abundances, *in situ*, iron

1 Introduction

The *in situ* observations of the solar wind charge state composition and elemental composition are vital tools in the investigation of the formation and origins of the solar wind. The charge state composition reflects thermal conditions encountered by solar wind plasma as it expands out through the solar corona and becomes constant past each ion's freeze-in point (Hundhausen et al., 1968; Hundhausen, 1968; 1972; Ko et al., 1997; Landi et al., 2012b; Rivera et al., 2022). Freeze-in distances for elements such as iron can range from 1 to 3 $R_\odot$ from the photosphere in the solar wind (Habbal et al., 2009; 2010; Boe et al., 2018)

or as far as 5 $R_\odot$ (Landi et al., 2012a; b) but can freeze-in as far as 10–25 $R_\odot$ in interplanetary coronal mass ejection (ICME)s (Rivera et al., 2019). Thus, the observations of solar wind charge state composition made *in situ* can be used to probe the various freeze-in conditions/heights to investigate the solar wind's formation.

The *in situ* observations of elemental abundances reflect the structures from which the solar wind originates. The solar wind abundances of low (<10 eV) first ionization potential (FIP) elements are fractionated, generally being enhanced above photospheric values, particularly in the slow solar wind. High (>10 eV) FIP elements are not enhanced above photospheric values, and elements such as neon and helium can even be depleted in the solar wind (Zurbuchen et al., 2016). This fractionation pattern, with low FIP elements enhanced above their photospheric values and high FIP elements consistent with their photospheric values, is known as the FIP effect. FIP fractionation in solar wind streams of varying speed has been related to coronal structures from which the solar wind originated (Geiss et al., 1995; von Steiger et al., 2000; Stakhiv et al., 2015; Zurbuchen et al., 2016; Zhao et al., 2017; Rivera et al., 2022). Fast streams with little to no fractionation are often associated with coronal holes, and slow streams with high fractionation are often associated with closed field regions (Stakhiv et al., 2015; Zurbuchen et al., 2016).

Theories for the mechanisms responsible for the FIP effect center around interactions between Alfve´n waves and ions/neutrals in the region between the upper chromosphere and base of the corona (Laming, 2015; Laming et al., 2019). These interactions lead to the separation (Lundin and Guglielmi, 2006) and preferential acceleration of low-FIP element ions from neutrals into the corona. Developing an understanding of the processes responsible for the FIP effect is considered central in determining the role of Alfve´n waves and turbulence in how the material is transported from the chromosphere into the solar corona and how the corona is heated (Laming, 2015; Laming et al., 2019).

Heavy ion composition has been observed *in situ* for decades using the solar wind ion composition sensor (SWICS) (Gloeckler et al., 1992) on Ulysses, SWICS (Gloeckler et al., 1998) on advanced composition explorer (ACE), plasma and suprathermal ion composition (PLASTIC) (Galvin et al., 2008) on the Solar Terrestrial Relations Observatory (STEREO), and more recently using the heavy ion sensor (HIS) in the solar wind analyzer (SWA) suite (Owen et al., 2020) on Solar Orbiter. These instruments have recorded heavy ion composition throughout multiple solar cycles (SC)s, and the similarity between the ions which ACE/SWICS and Solar Orbiter/HIS observe can allow for comparisons between current and past SCs. Livi et al. (2023) compared iron abundances relative to oxygen (Fe/O), oxygen, and carbon charge state ratios (O^{7+}/O^{6+} and C^{6+}/C^{5+}, respectively) and the speed of O^{6+} ions measured by HIS from January to December of 2022 to similar ACE/SWICS measurements ranging from February 1998 to August 2011. Measurements by HIS currently range up through most of the ascending phase of SC 25, and charge state composition measurements include O^{5-8+} and Fe^{8-12+} ions, which are also observed by SWICS. Because of this, there is an opportunity to compare the heavy ion composition measured in the solar wind in isolated ascending phases of two different SCs in terms of individual ions and elemental abundances.

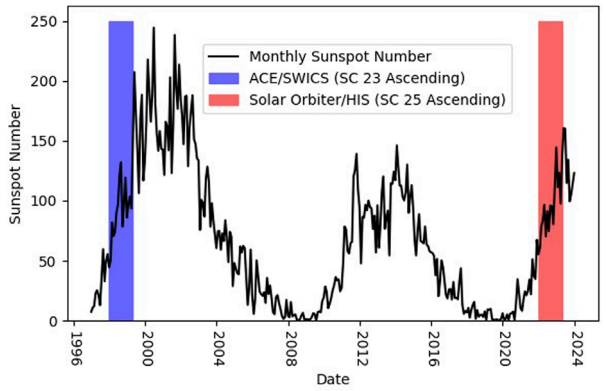

FIGURE 1
Monthly sunspot numbers between 1996 and 2024, as well as selected time ranges for the ACE (blue) and Solar Orbiter (red) data.

In this work, we seek to answer how the solar wind composition changed between the ascending phases of SCs 23 and 25. In Section 2, we describe the ACE and Solar Orbiter observations used in the analysis. In Section 3, we compare the solar wind composition in these two ascending phases in terms of the iron and oxygen charge state composition (Section 3.1), iron abundances relative to oxygen, and how contributions of individual ions impact the aggregate elemental abundance (Section 3.2). In Section 4, we discuss implications for the conditions in the corona across these time periods. In Section 5, we describe our conclusion.

2 Observations

Figure 1 shows the provisional international sunspot numbers (Ri) (SIDC-Team et al., 1981) between 1996 and 2024. The Solar Orbiter/HIS observational period extends from January 2022 to April 2023, part of the SC 25 ascending phase. Loosely matching the sunspot numbers is the selected ACE/SWICS observational period, which extends from January 1998 to April 1999—the latter part of the SC 23 ascending phase. In these selected time ranges, the HIS measurements span approximately 16 months, and the ACE/SWICS measurements span approximately 15 months, only beginning in February 1998. Although the 1.1 version of the ACE/SWICS level 2 observations span up to August 2011, the relative levels of activity during the SC 24 ascending phase make it more challenging to compare to the SC 23 and 25 ascending phases. The HIS L3 composition data (Müller et al., 2020; Owen et al., 2020; Livi et al., 2023) contain measurements of elemental abundances and charge state composition of a subset of ions and elements in the solar wind. The iron abundance (Fe/O), iron charge state distribution (Fe^{8-12+}), and oxygen charge state distribution (O^{5-8+}) are observed at a 10-min resolution and, in this work, are taken from January 2022 to April 2023. We use bulk proton speed observations from proton and alpha particle sensor (PAS) (Owen et al., 2020) L2 ground moment data (Müller et al., 2020) re-timed to the 10-min resolution of HIS to bin the composition data by proton speed.

The solar wind heavy ion composition measurements are taken from SWICS (Gloeckler et al., 1998) level 2 data, version

1.1 (Shearer et al., 2014; Raines et al., 2005). We select the iron abundance (Fe/O), iron charge state composition (Fe^{6-20+}), and oxygen charge state composition (O^{5-8+}) measurements at a 2-h time resolution. The charge state composition is recorded in charge state distributions: arrays of each observed ion's charge state fraction or density of the ion relative to the density of the element as a whole. In other words, charge state distributions represent the densities of individual observed ions, normalized to the total elemental density. Since the iron charge state distribution in the HIS data does not include Fe^{6-7+} and Fe^{13-20+}, we select only the Fe^{8-12+} charge states from the ACE/SWICS iron charge state distribution. We then re-normalize each observation to the sum of the Fe^{8-12+} charge state fractions. Iron abundances relative to oxygen will not be normalized since the Fe/O ratio measured by HIS includes the Fe^{6-20+} and O^{5-8+} charge states, similar to ACE. Any measurement with a quality flag other than 0, the flag for good data, is considered a missing value and excluded from calculations. Additionally, any charge state fraction with an associated statistical error greater than 0.4 (40%) is also excluded. We use the bulk proton speed observations from solar wind electron proton alpha monitor (SWEPAM) (McComas et al., 1998) level 2 data (Garrard et al., 1998) re-timed to the 2-h time resolution of SWICS to bin the composition data by proton speed.

Monthly accumulated wind speed histograms (top) and sunspot numbers (bottom) are shown in Figure 2. Solar Orbiter/PAS (right) made more observations of wind moving at higher speeds than ACE/SWEPAM (left) did, with some monthly histograms even ranging between 750 and 800 km s^{-1}. There are some notable peaks in the 300–350 km s^{-1} and 350–450 km s^{-1} range as well, where Solar Orbiter measured a relatively high amount of samples in that monthly period. If we define the fast wind as having proton speeds greater than 500 km s^{-1} and the slow wind as having proton speeds less than this, about 13% of the ACE data are attributed to the fast wind and 87% of the data are attributed to the slow wind. By similar metrics, Solar Orbiter encountered a larger proportion of fast wind observations at 32%, with about 68% of the data being attributed to the slow wind. The monthly sunspot numbers in these ascending phases are comparable, starting at approximately 50 sunspots at the beginning of the observation period and ending near 150 sunspots.

Since the composition of the solar wind material associated with ICMEs can differ significantly from the nominal solar wind (Zurbuchen et al., 2016; Richardson and Cane, 2010), we seek to mitigate the influence of ICME material on our analysis. In the ACE data, intervals of the ICMEs identified by Richardson and Cane (2010) and Jian et al. (2011), along with a buffer surrounding these intervals from 48 h before to 48 h after the ICME intervals, are not considered in our calculations. A similar list of ICMEs has not yet been published for Solar Orbiter. Instead, we apply a scheme from Richardson and Cane (2004) and later Zhao et al. (2009) using a combination of the proton speed and the O^{7+}/O^{6+} ratio to remove possible ICME data. The ICME samples are flagged using Equation 1:

$$\frac{O^{7+}}{O^{6+}} \geq 6.008e(-0.00578V_{SW}), \quad (1)$$

where V_{SW} is the solar wind bulk proton speed. If the Equation 1 is true, the sample is considered ICME wind. A buffer surrounding potential ICME samples is not used, and Equation 1 has not been validated for the Solar Orbiter measurements, which will be discussed in Section 4.

3 Analysis

3.1 Fe and O charge state composition

To analyze the charge state composition in these ascending phases, we first examine the average iron and oxygen charge state distributions across different solar wind speeds. The charge state fractions of the iron and oxygen ions are binned using proton speed data into six bins ranging from 200 to 800 km s^{-1}, as shown in the first column of Table 1. The other two columns in Table 1 show the sample sizes in each wind speed bin for both ascending phases, following ICME removal. Most observations are within the 300–600-km s^{-1} range. The 600–800 km s^{-1} range effectively includes all observations measured at wind speeds greater than 600 km s^{-1} since neither spacecraft recorded non-ICME composition measurements at associated speeds above 800 km s^{-1}.

Figure 3 shows the wind speed dependency of the averaged iron (top row) and oxygen (bottom row) charge state distributions. Each cell is colored using a logarithmic base 10 norm to visualize the orders of magnitude, in which the charge state fractions vary. The general wind speed dependency of the averaged charge state distributions is similar between the ACE/SWICS data (left column of panels) and the Solar Orbiter/HIS data (right column of panels). The contributions from individual iron ions to the total iron density do not appear to have any regular wind speed dependency, evidenced by no charge state monotonically increasing or decreasing with higher wind speed bins. The contributions of Fe^{11+} and Fe^{12+} to the total iron density measured during the ascending phase of cycle 23 (left) are slightly lower than they are in the ascending phase of cycle 25 (right), and the contributions from Fe^{8+} and Fe^{9+} are generally higher. The contributions from individual oxygen ions to the total oxygen density appear to have a similar wind speed dependency between both ascending phases, with the O^{6+} charge states contributing more at higher wind speeds and the O^{7+} and O^{8+} charge states contributing less. The contribution of individual ions again differs only slightly between the ascending phases of cycles 23 and 25, but Solar Orbiter measured solar wind plasma, which had higher contributions of O^{7+} and lower contributions of O^{6+} than ACE did at speeds greater than 600 km s^{-1}.

The O^{7+}/O^{6+} ratio, which describes the relative contribution of the O^{6+} and O^{7+} ions to the total oxygen density, is a signature which indicates the source of the solar wind plasma (e.g., Zurbuchen et al., 2002; Zhao et al., 2009; 2014; 2017)). Figure 4 shows the medians and interquartile ranges of the O^{7+}/O^{6+} ratio, separated into the same wind speed bins as Figure 3, but also includes ACE/SWICS measurements during the sunspot maximum of SC 23 (01/2000–12/2002) and the descending phase of SC 23 (01/2003–04/2004) to examine any possible solar cycle-related effects. In the SC 23 ascending phase, between 200 and 400 km s^{-1}, the median O^{7+}/O^{6+} measured by ACE/SWICS exceeds that measured by Solar Orbiter/HIS, but the interquartile ranges indicate this excess may not be necessarily significant. In the SC 25 ascending phase (the Solar Orbiter/HIS observations), the solar wind O^{7+}/O^{6+} ratio is notably higher than it is in the SC 23 ascending phase (the ACE/SWICS observations) at wind speeds between 600 and 800 km s^{-1}. In the same wind speed bin, the Solar Orbiter/HIS O^{7+}/O^{6+} ratio almost completes overlaps when compared to those made by ACE/SWICS during the SC 23 Solar maximum and

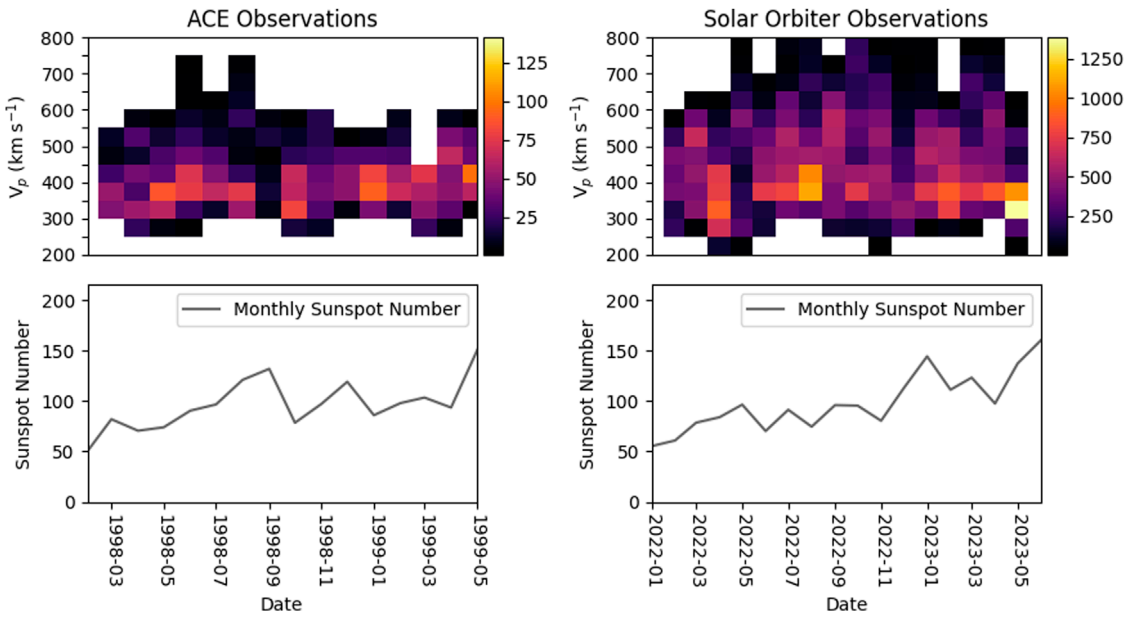

FIGURE 2
Monthly proton speed histograms and sunspot numbers during the selected ascending phases of SCs 23 (ACE observations, left) and 25 (Solar Orbiter observations, right).

TABLE 1 Statistical non-ICME sample size within each speed bin for the ACE/SWICS (SC 23 ascending phase) and Solar Orbiter/HIS (SC 25 ascending phase) observations.

Speed range (km s^{-1})	ACE/SWICS (2 h)	Solar Orbiter/HIS (10 min)
200–300	88	2,611
300–400	1,405	18,236
400–500	1,126	14,382
500–600	350	10,786
600–800	32	5,331

overlaps by approximately 50% of the observations in the SC 23 descending phase. This could suggest that in the SC 25 ascending phase, the solar wind plasma in the fastest streams originated from regions in closer proximity to sources where the plasma was highly ionized, such as helmet streamers and coronal holes, than it did during the SC 23 ascending phase. This point will be revisited in Section 4.

Since the wind speed dependency of the averaged iron and oxygen charge state distributions was generally similar between both ascending phases, we separated the charge state composition measurements into traditionally defined fast (V_p > 500 km s^{-1}) and slow (V_p < 500 km s^{-1}) winds. From Table 1, there are 2,619 slow wind and 382 fast wind non-ICME observations during the SC 23 ascending phase and 35,229 slow wind and 16,117 fast wind non-ICME observations during the SC 25 ascending phase. To check if these similarities were unique to the ascending phase, we again examined the ACE/SWICS measurements during the sunspot maximum of SC 23 (01/2000–12/2002) and the descending phase of SC 23 (01/2003–04/2004).

Figure 5 shows the averaged iron (top) and oxygen (bottom) charge state distributions, with error bars spanning 1 standard deviation from the mean to convey the variability of individual observations. Each column corresponds to the phase of the SC labeled in the iron charge state distribution panels. The iron charge state distribution in the slow solar wind (red) appears to remain similar across the different phases of the SC, peaking at Fe^{9+}, with the contributions from other charges states appearing constant across all phases. However, the composition observed in the fast solar wind (blue) seems to have a cycle dependency.

In the ascending phases, the fast wind iron charge state distribution peaks at the Fe^{9+} charge state, but in solar maximum and the descending phase of cycle 23, the fast wind iron charge state distribution peaks at Fe^{10+}. The oxygen charge state composition does not exhibit a significant solar cycle dependency in either the fast or slow solar wind streams.

FIGURE 3
Averaged charge state distributions of iron (top row) and oxygen (bottom row) ions, observed by ACE/SWICS (left column) and Solar Orbiter/HIS (right column). Cells are annotated with average values of the charge state fractions and are color-coded by the logarithmic base 10 norm of the averages.

3.2 Iron abundances and individual ion ratios

To analyze the solar wind elemental composition during these ascending phases, we first examine the abundance of iron relative to oxygen, in terms of FIP fractionation. The photospheric abundances are taken from Caffau et al. (2011) and are converted to Fe/O using Equation 2:

$$\left(\frac{n_{Fe}}{n_O}\right)_{photo} = \frac{10^{A_{Fe}-12}}{10^{A_O-12}} = 10^{A_{Fe}-A_O}, \quad (2)$$

where A_{Fe} and A_O are the photospheric abundances of iron and oxygen on a logarithmic scale, with the hydrogen abundance defined as 12. Here, A_{Fe} = 7.50 and A_O = 8.83, with Fe/O$_{photo}$ ≈ 0.0468. We divide the solar wind measurements of Fe/O by Fe/O$_{photo}$ to determine the FIP fractionation for each observation.

Figure 6 shows the median iron FIP fractionation and interquartile ranges of the ascending phases observed by ACE and Solar Orbiter. The upper error bars are somewhat longer than the lower ones, indicating that Fe/O measurements in both the fast and slow wind are slightly skewed toward higher abundances. There is no significant difference in slow wind FIP fractionation between the ascending phases of SCs 23 observed by ACE and 25 observed by Solar Orbiter, but in the fast wind, the median FIP fractions in the Solar Orbiter observations are nearly within the upper quartile of the ACE observations. This implies that a majority of the Fe/O observations during the ascending phase of cycle 25 originating from high wind speed sources were more highly fractionated than similar observations made during the ascending phase of cycle 23.

Since the iron abundances relative to oxygen represent the aggregate densities of each identified ion, we then seek to answer how the contributions of individual ions can impact iron fractionation. To do this, we examine individual ion ratios, calculated using iron and oxygen charge state fractions using Equation 3:

$$\frac{\mathrm{Fe}^{*+}}{\mathrm{O}^{*+}} = \frac{\mathrm{Fe}}{\mathrm{O}} \times \frac{\frac{\mathrm{Fe}^{*+}}{\mathrm{Fe}}}{\frac{\mathrm{O}^{*+}}{\mathrm{O}}}. \quad (3)$$

After the individual ion ratios are calculated, the data are once again separated into fast (V_p>500 km s^{-1}) and slow (V_p<500 km s^{-1}) wind. Like in the previous case, we normalize the solar wind observations of Fe/O to the photospheric equivalent (Equation 2) to compute the FIP fractionation of the individual ion ratios. We appreciate that the individual ion ratios are not necessarily reflected in the photospheric abundances of iron;

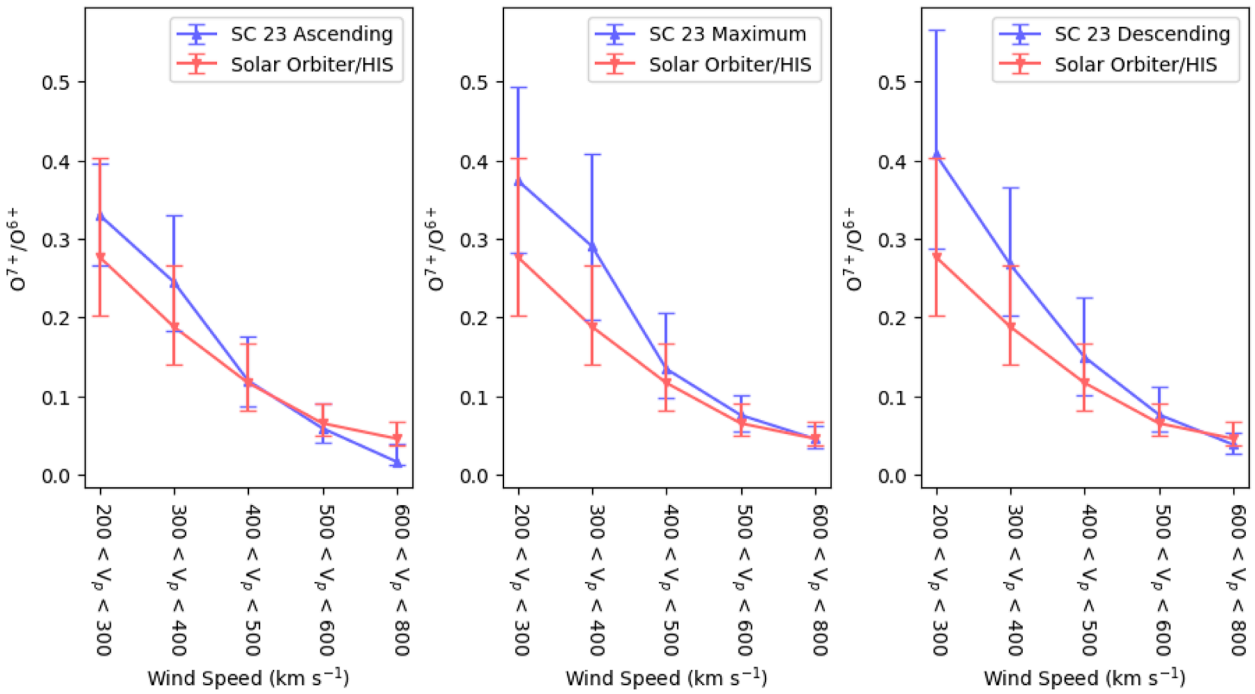

FIGURE 4
Median and interquartile ranges of the O^{7+}/O^{6+} ratio observed by ACE/SWICS (blue, upward triangle markers) during the ascending, maximum, and descending phases (left, middle, and right, respectively) of SC 23, as well as Solar Orbiter/HIS (red, downward triangle markers).

rather, we are assuming the solar wind abundances of iron and oxygen are completely composed of the ions which form the ratio for the sake of comparison.

Figure 7 shows the medians and interquartile ranges of the FIP fractionation of aggregate iron abundances and individual ion ratios, as observed by ACE/SWICS (top) and by Solar Orbiter/HIS (bottom). The dashed line denotes the photospheric abundances. The FIP fractionation of individual ion ratios varies significantly from the aggregate elemental abundance, with some ratios being multiple orders of magnitude greater than the Fe/O FIP fractionation. The individual ion ratios exhibit patterns dependent on which iron and oxygen ions are included in the ratio: ratios of Fe^{*+}/O^{8+} are greatly enhanced compared to Fe/O, whereas ratios of Fe^{*+}/O^{6+} are depleted, with the latter appearing depleted in the solar wind when compared to the photosphere. The order of predominance in the fast and slow wind also seems dependent on the oxygen charge state: the Fe^{*+}/O^{5+} and Fe^{*+}/O^{6+} ratios are, in general, slightly more predominant in the slow wind than in the fast wind. For the Fe^{*+}/O^{7+} and Fe^{*+}/O^{8+} ratios, this ordering is reversed: the fast wind values dominate the slow wind values. The error bars indicate that the fast and slow wind are more separable for Fe^{*+}/O^{7+} and Fe^{*+}/O^{8+}; even in the Solar Orbiter data, where the slow wind Fe/O almost completely overlaps the fast wind, like what is shown in Figure 6. The Solar Orbiter/HIS individual ion ratios generally exhibit similar patterns to those from the ACE/SWICS observations but with some ratios being noticeably higher or lower. The fast wind Fe^{*+}/O^{8+} are lower at Solar Orbiter/HIS than they are at ACE/SWICS, and almost all other ratios seem higher or about equivalent. The Fe^{12+}/O^{7+} ratio seems particularly unique; although the Fe^{12+}/O^{7+} ratio in the Orbiter/HIS observations is FIP enhanced, the same ratio in the ACE/SWICS observations is only enhanced in the fast wind and is depleted in the slow wind.

To summarize, we compare the iron and oxygen charge state composition and iron abundances relative to oxygen measured during the ascending phases of SCs 23 and 25, using the ACE/SWICS and Solar Orbiter/HIS observations. Some of the most significant findings from this analysis include the following:

- Iron ions do not exhibit a significant wind speed dependency, but there are slight differences in some of the Fe ion contributions. The oxygen ions do exhibit some wind speed dependency, where contributions from O^{6+} increase and contributions from O^{7+} and O^{8+} decrease in the transition to higher wind speeds.
- The solar wind O^{7+}/O^{6+} ratio is higher during the SC 25 ascending phase than it is during the SC 23 ascending phase with wind speeds ranging from 600 to 800 km s^{-1}.
- The iron charge state composition in the slow solar wind appears similar across different phases of the SC, but in the fast wind, there is an appreciable shift in the iron charge state distribution: in the ascending phases, the iron distribution peaks at Fe^{9+}, but in the maximum and descending phase, it peaks at Fe^{10+}. The oxygen charge state distribution did not appear to have a significant solar cycle dependency.
- The iron abundances relative to oxygen appear to be equally fractionated in the slow solar wind, but in the fast wind, iron was more fractionated in the ascending phase of SC 25 than it was in the ascending phase of SC 23.

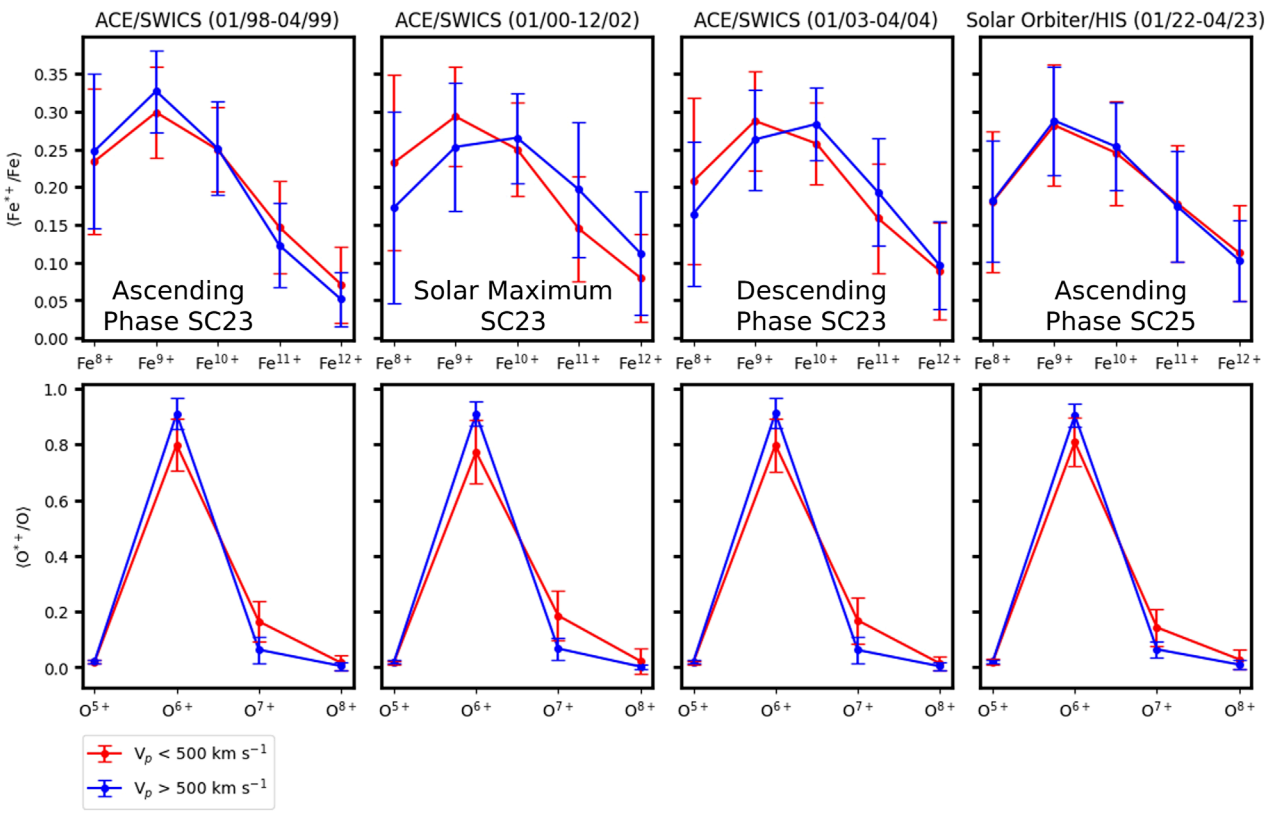

FIGURE 5
Iron (top row) and oxygen (bottom row) averaged charge state distributions in the slow (red) and fast (blue) wind, observed by ACE/SWICS in the ascending phase (first column), solar maximum (second column), and descending phase (third column) of SC 23, as well as the ascending phase of SC 25 (fourth column). The error bars denote one standard deviation from the average.

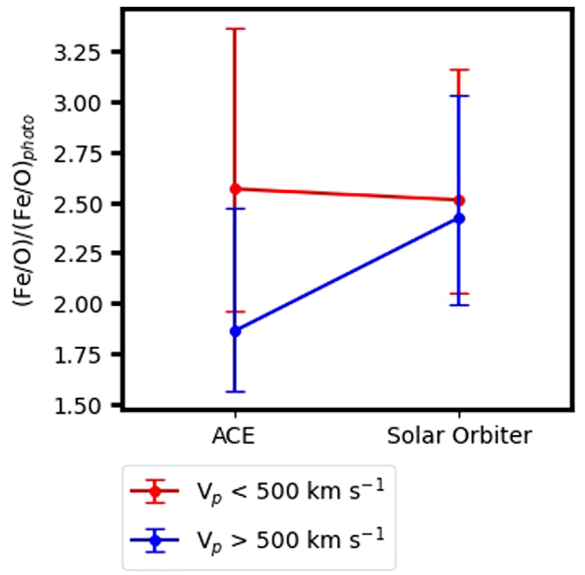

FIGURE 6
Comparison of iron fractionation in slow (red) wind and in fast (blue) wind between ACE/SWICS and Solar Orbiter/HIS. Markers indicate medians, and error bars denote the interquartile range.

- The FIP fractionation of individual ion ratios can vary significantly from the aggregate elemental abundance. The $Fe*^{+}/O^{7+}$ and $Fe*^{+}/O^{8+}$ ratios appear more separable between the fast and slow wind when compared to Fe/O.

4 Discussion

The wind speed dependency of iron and oxygen ions is mostly similar between the two ascending phases examined; however, there were slight differences in the average contributions of ions. The higher charge states of Fe^{11-12+} and O^{7-8+} were measured in greater abundance in SC 25 than they were in SC 23. Simultaneously, Fe^{8-9+} and O^{6+} contributed less in the ascending phase of SC 25 than they did in the ascending phase of cycle 23, with the lower contributions from O^{6+} at speeds greater than 400 km s^{-1} and the lower contributions from Fe^{8-9+} at all wind speeds, on average. In terms of the thermal conditions which determined these ionization states, this could indicate that the Solar Orbiter observed material which encountered slightly higher electron temperatures than ACE did during the ascending phase it observed, assuming electron and ion density profiles remained generally similar at their sources and that the solar wind speed remained mostly constant

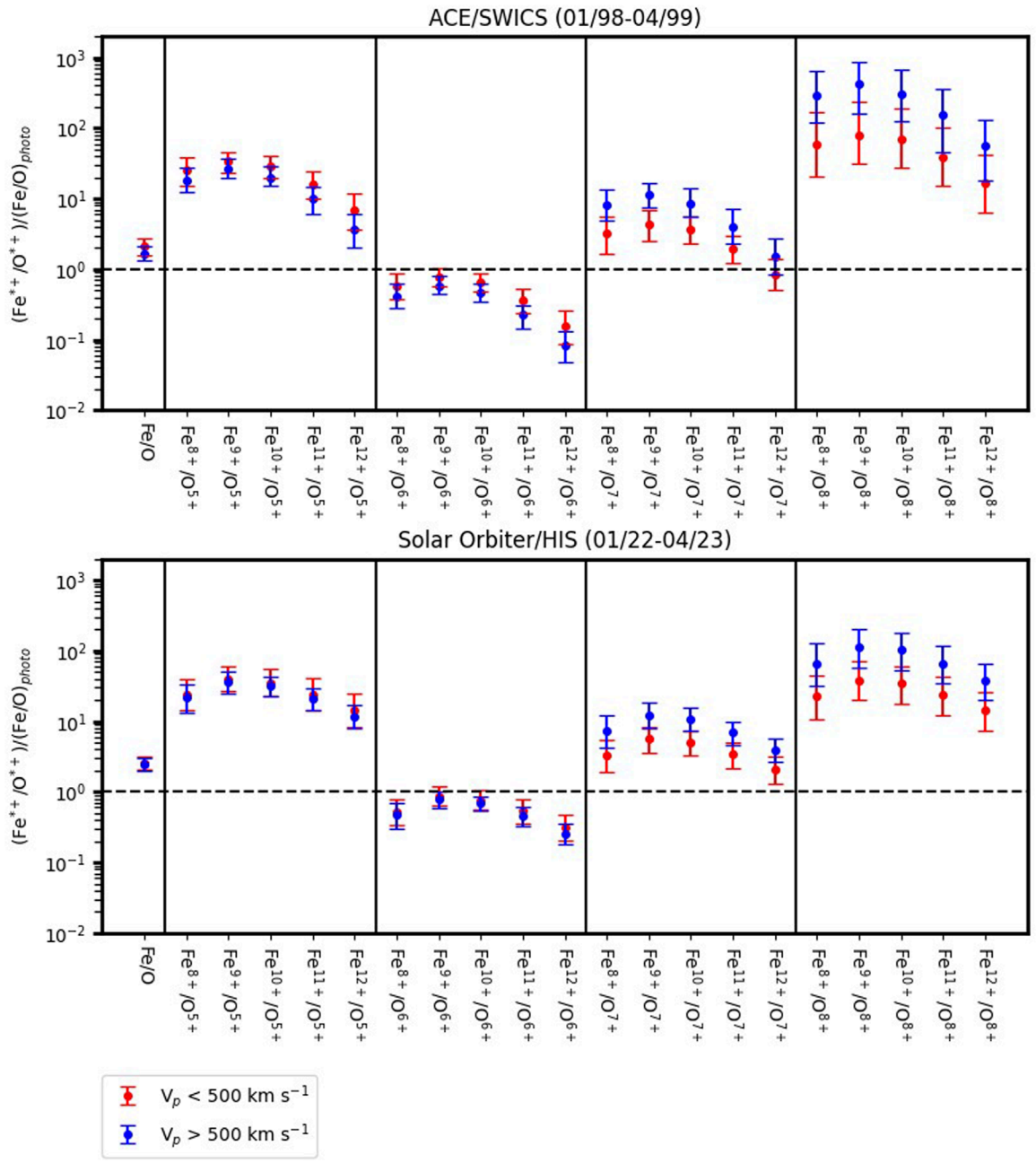

FIGURE 7
Comparison of the median and interquartile ranges of Fe/O and individual ion ratio (Fe^{*+}/O^{*+}) fractionation between ACE/SWICS (top) and Solar Orbiter/HIS (bottom). The red series represents the slow (V_p < 500 km s^{-1}) wind, and the blue series represents the fast (V_p > 500 km s^{-1}) wind. The dashed line is where the Fe/O fractionation is equal to 1.

past the corona. Models predict that high charge states generally freeze-in at lower altitudes than low charge states, and oxygen ions generally freeze-in before iron ions (Gilly and Cranmer, 2020). It could be the electron temperatures at the Fe^{8-9+} freeze-in height were higher during the SC 25 ascending phase than they were during the SC 23 ascending phase. Another possibility is that Solar Orbiter encountered more boundary wind than ACE did, reinforced by the fact that Solar Orbiter/HIS observed higher contributions of O^{7+} and lower contributions of O^{6+} than ACE/SWICS did at speeds between 600 and 800 km s^{-1}. We will revisit this point when we discuss the elemental abundances of iron.

The iron charge state composition in the fast wind varied as the sunspot number increased, to the point where in solar maximum the iron charge distribution peaked at Fe^{10+}, as opposed to Fe^{9+} in the ascending phases; however, in the descending phase, the peak remained at Fe^{10+}. Assuming these fast wind streams originated around equatorial coronal holes, this could indicate that thermal conditions where iron freezes-in changed with the sunspot number.

These thermal conditions include electron temperature, electron density, ion density, and the time spent in the ionization region, the last of which is relatively low in fast-speed streams. These changes in thermal conditions coincide with greater numbers of sunspots, which, in turn, are responsible for the active regions where solar plasma can become highly ionized. It is possible that as the number of active regions increases, the equatorial coronal hole fields may more frequently reconnect with active region fields and transport this highly ionized plasma; however, the persistently high contributions of Fe^{10+} in the declining phase, in conjunction with significant differences between the fast and slow wind Fe/O fractionation suggest this might not be the case. The iron charge state composition in the slow wind remained unaffected as the sunspot number varied, indicating that the number of active regions did not have an effect on the relative contributions of Fe^{9+} and Fe^{10+}.

The aggregate iron abundances make this picture more complicated. In the Solar Orbiter/HIS observations made during the ascending phase of cycle 25, nearly 50% of the fast wind iron fractionation was as high as the slow wind, judging by the interquartile range in Figure 6. There are a few scenarios which could explain this, the most likely of which is that there is a significant amount of ICME material still included in the Solar Orbiter/HIS data. In hot ICMEs originating from long-lived loops or active regions, the magnetic cloud can contain highly fractionated iron (Zurbuchen et al., 2016). If our method to exclude possible ICME material was insufficient in doing so, the fast wind from the ICME material would be highly fractionated, appearing similar to the slow wind. This is possible since our method of excluding ICMEs using both the O^{7+}/O^{6+} charge state ratio and the proton speed (Equation 1) was not applied to the ACE data and has not been tested using the Solar Orbiter/HIS data. Unfortunately, lack of $Fe^{14\sim16+}$ observations in the current version of the Solar Orbiter/HIS L3 composition data (Livi et al., 2023) makes it difficult to determine the presence of the ICME material through the charge state distributions alone (Lepri and Zurbuchen, 2004). If the ICME material was the cause of these highly fractionated fast wind iron measurements, then the identification technique would thus need to be refined, either through adjustment of the variable thresholds in Equation 1, or the inclusion of other parameters which together could more reliably flag potential ICME wind.

If we assume the ICME material had been adequately removed from the Solar Orbiter/HIS data, then we must raise the question as to why the iron abundances originating from fast wind sources during these two ascending phases were so different. The slow wind is known to have a large degree of variability when it comes to iron fractionation, containing iron abundances as low as the wind originating from coronal holes (Stakhiv et al., 2015; 2016; Livi et al., 2023). In their unified wind scenario, Stakhiv et al. (2016) concluded that highly fractionated iron in slow wind streams originates from coronal loops which allow iron to achieve higher levels of fractionation. Solar wind plasma streaming at speeds in excess of 500 km s^{-1} is expected to originate from coronal holes with less fractionated iron, such as what was confirmed using Ulysses composition data (Stakhiv et al., 2015); however, Solar Orbiter also appeared to, on average, be generally more frequently connected to fast wind streams than ACE was during these time periods, as shown in Figure 2, and yet, the iron fraction was unexpectedly high, matching the slow wind fractionation. This also places the fast wind observations in contrast with the proposed boundary wind, which is expected to move at relatively low speeds, but have similar elemental fractionation to those of fast wind sources (Stakhiv et al., 2015). A dependency on solar activity could be largely ruled out since iron abundances in wind originating from coronal holes are not expected to change drastically with the solar cycle phase, unlike helmet streamers (Zhao et al., 2017); however, Zhao and Landi (2014) found that the Fe/O ratio of the solar wind originating from equatorial coronal holes increased drastically when comparing the solar minimum between SC 22 and 23 and the solar minimum between SC 23 and 24. Once again assuming the observations in this present work originate from equatorial coronal holes, the highly fractionated fast wind, in conjunction with the relatively high O^{7+}/O^{6+} ratio, could suggest the fast speed winds which reached Solar Orbiter originated from coronal hole magnetic fields reconnecting with structures such as active regions. In a sense, the fast wind plasma measured Solar Orbiter/HIS may have been mostly mixed with slow wind sources. Additionally, once Solar Orbiter reaches a trajectory of roughly 33° solar latitude (Müller et al., 2020), it is possible that the compositional characteristics from coronal holes and streamer regions could be more accurately distinguished, even by bulk wind speed.

In this work, we do not account for distance from the Sun in our comparison since the charge state composition is considered non-evolving past each individual ion's freeze-in point, due to the density of the solar wind being too low to allow for ionization or recombination processes to continue, which prevents both the charge state ratios and the individual ion charge state fractions from changing. The exception to this is when the material is contained within an ICME, which can result in freeze-in distances much farther than typical, but ideally, such ICME material would be fully excluded from this analysis. Another means by which solar wind composition may vary due to turbulence is in the case of the Alfvénic slow solar wind, which has been shown to have compositional properties similar to that of coronal holes, with such cases being the subject of future work.

There is a great deal of variability in the ion ratios between two different elements—none of the ion ratios computed using Equation 3 closely match the aggregate elemental abundance for both the fast and slow solar wind. However, these ratios do provide a spectrum to analyze the aggregate elemental abundance. The oxygen ion density, being in the denominator of Equation 3, seems to greatly affect the magnitude of the individual ion ratios: O^{6+} being largely dominant effectively lowers its group of ion ratios, whereas O^{8+}, being extremely low in abundance *in situ*, seems responsible for the apparent enhancement for its group. Individual ion ratios can show much larger differences between the fast and slow wind when compared to the fractionation of the aggregate elemental abundance, despite being proportional to it. This is important as the densities of individual ions comprise the aggregate elemental abundance, suggesting that the inclusion of many ions is required to adequately capture the behavior of the element. For instance, excluding the O^{5+} density from the observations would be removing a small fraction of the oxygen species, but ratios against O^{5+} are some of the only ones which exhibit the standard ordering of predominance of the fast and slow wind, similar to Fe/O. This could also suggest that the Fe/O observations could change once more iron ion species have been identified, possibly better reflecting the ACE/SWICS data. Although they may be useful for analysis involving differential speeds and mass-proportional temperatures, the Ulysses/SWICS data documentation even cautions against deriving freeze-in temperatures or abundance ratios of elements

from individual ion ratios as they offer ion densities relative to O^{6+} (Zurbuchen and von Steiger, 2011). The present work demonstrates that such ion densities are expected to be depleted when compared to aggregate elemental abundances when multiple iron and oxygen charge states are sampled.

From this, we posit that future investigations operating with a limited subset of ion species take caution in the interpretation of results when applied to the aggregate as the exclusion of even less common charge states could affect the behavior of the aggregate elemental abundance. For instance, the previously mentioned Ulysses/SWICS observations only identify Fe^{6-16+} and O^{6-8+} charge states in their iron and oxygen charge state distributions, respectively. The reported aggregate elemental abundance might thus be biased when compared to the ACE/SWICS observations of the same type as ACE has identified ions for the Fe^{6-20+} and O^{5-8+} charge states in their iron and oxygen charge state distributions.

In future releases of Solar Orbiter/HIS data, the model for identifying elements and charge states will have been refined, allowing for the inclusion of other ions which can be used as signatures for the origins and formation history of the solar wind. Despite having normalized the iron charge state distribution in the analysis of this present work, we find from these results that enhanced forward modeling and ion extraction may yield a more accurate comparison. The inclusion of magnesium and silicon—other low-FIP elements with ions possessing several charge states identified *in situ* as well as the full set of identified iron ions, will be crucial in verifying that ICME material is being sampled. The additional elemental abundances of low-FIP elements will reveal if iron fractionation in the ascending phase of SC 25 is unique or if the highly fractionated material was truly present in fast-wind streams.

5 Conclusion

In this work, we compare the solar wind heavy ion composition during the ascending phase of SCs 23 and 25. We first compared the wind speed dependency of the iron and oxygen charge state composition. We found that iron ions do not exhibit a wind speed dependency, while the oxygen ions do. Slight differences in ion contributions between these two ascending phases might suggest subtle changes in the conditions encountered in higher speed source regions, particularly at the freeze-in point of iron. We also compared the iron and oxygen charge state composition in the traditionally defined fast and slow wind, including observations from solar maximum and the descending phase of SC 23 in the comparison. Although the iron composition in the slow solar wind did not appear to have a solar cycle dependency, the peak of the iron distribution in the fast wind shifted to a higher charge state in the maximum and descending phase than it was in either ascending phases. The contributions from oxygen ions do not appear to have a significant solar cycle dependency. We compared the elemental composition between the ascending phases by first examining the FIP fractionation of iron, which we found to be equally fractionated in the slow wind; however, in the fast solar wind, iron was more fractionated in the ascending phase of SC 25 than it was during the ascending phase of SC 23, and in conjunction with an enhanced O^{7+}/O^{6+} ratio in the SC 25 ascending phase, it suggests that many high speed streams in SC 25 were the result of coronal hole magnetic fields frequently reconnecting with slow wind sources. To determine the impact of the contributions of individual ions on the aggregate elemental abundance, we compared individual ion ratios to the aggregate elemental abundances in terms of an analogous FIP fractionation. We find that the individual ion ratios exhibit a high degree of variability and show particular differences in the fast and slow solar wind, leading us to conclude that the exclusion of even less common charge states could affect the behavior of the aggregate elemental abundance. Further investigation should be made once forward modeling enables the extraction of a wider array of iron charge states, along with the inclusion of magnesium and silicon elemental abundances and charge state composition.

Data availability statement

Publicly available datasets were analyzed in this study. The ACE data can be found at the ACE Science Center (ASC): https://izw1.caltech.edu/ACE/ASC/. The Solar Orbiter data can be found at the Solar Orbiter Archive: https://soar.esac.esa.int/soar/.

Author contributions

DC: Conceptualization, Formal analyis, Investigation, Methodology, Visualization, Writing–original draft, Writing–review and editing. STL: Conceptualization, Funding acquisition, Methodology, Project administration, Resources, Supervision, Validation, Writing–original draft, Writing–review and editing. LZ: Conceptualization, Funding acquisition, Methodology, Project administration, Resources, Supervision, Validation, Writing–original draft, Writing–review and editing. RD: Supervision, Validation, Writing–review and editing. JR: Supervision, Validation, Writing–review and editing. SL: Supervision, Validation, Writing–review and editing. AG: Supervision, Validation, Writing–review and editing. LK: Supervision, Validation, Writing–review and editing.

Funding

The author(s) declare that financial support was received for the research, authorship, and/or publication of this article. LZ acknowledges support from NASA grants (80NSSC21K0579 and 80NSSC22K1015), NSF SHINE grant (2229138), and NSF Early Career grant (2237435). STL, RD, JR and SL were supported by NASA contract NNG10EK25C for work on HIS. STL and JR were also supported by NASA contract 80NSSC23K0542 for work on ACE/SWICS.

Conflict of interest

The authors declare that the research was conducted in the absence of any commercial or financial relationships that could be construed as a potential conflict of interest.

Publisher's note

References

Boe, B., Habbal, S., Druckmu¨ller, M., Landi, E., Kourkchi, E., Ding, A., et al. (2018). The first empirical determination of the fe10+ and fe13+ freeze-in distances in the solar corona. *Astrophysical J.* 859, 155. doi:10.3847/1538-4357/aabfb7

Caffau, E., Ludwig, H.-G., Steffan, M., Freytag, B., and Bonifacio, P. (2011). Solar chemical abundances determined with a co5bold 3d model atmosphere. *Sol. Phys.* 268, 255–269. doi:10.1007/s11207-010-9541-4

Galvin, A. B., Kistler, L. M., Popecki, M. A., Farrugia, C. J., Simunac, K. D. C., Ellis, L., et al. (2008). The plasma and suprathermal ion composition (plastic) investigation on the stereo observatories. *Space Sci. Rev.* 136, 437–486. doi:10.1007/s11214-007-9296-x

Garrard, T., Davis, A., Hammondn, J., and Sears, S. (1998). The ace science center. *Space Sci. Rev.* 86, 649–663. doi:10.1023/A:1005096317576

Geiss, J., Gloeckler, G., and Von Steiger, R. (1995). Origin of the solar wind from composition data. *Space Sci. Rev.* 72, 49–60. doi:10.1007/BF00768753

Gilly, C., and Cranmer, S. (2020). The effect of solar wind expansion and nonequilibrium ionization on the broadening of coronal emission lines. *Astrophysical J.* 901, 150. doi:10.3847/1538-4357/abb1ad

Gloeckler, G., Cain, J., Ipavich, F., Tums, E., Bedini, P., Fisk, L., et al. (1998). Investigation of the composition of solar and interstellar matter using solar wind and pickup ion measurements with swics and swims on the ace spacecraft. *Space Sci. Rev.* 86, 497–539. doi:10.1023/A:1005036131689

Gloeckler, G., Geiss, J., Balsiger, H., Bedini, P., Cain, J., Fischer, J., et al. (1992). The solar wind ion composition spectrometer. *Astronomy Astrophysics Suppl. Ser.* 92, 267–289.

Habbal, S. R., Druckmu¨ ller, M., Morgan, H., Daw, A., Johnson, J., Ding, A., et al. (2009). Mapping the distribution of electron temperature and fe charge states in the corona with total solar eclipse observations. *Astrophysical J.* 708, 1650–1662. doi:10.1088/0004-637X/708/2/1650

Habbal, S. R., Morgan, H., Druckmu¨ ller, M., and Ding, A. (2010). On the constancy of the electron temperature in the expanding corona throughout solar cycle 23. *Astrophysical J. Lett.* 711, L75. doi:10.1088/2041-8205/711/2/L75

Hundhausen, A. (1968). Direct observations of solar-wind particles. *Space Sci. Rev.* 8, 690–749. doi:10.1007/BF00175116

Hundhausen, A. J. (1972). *Coronal expansion and solar wind*. Berlin, Heidelberg: Springer.

Hundhausen, A. J., Gilbert, H. E., and Bame, S. J. (1968). Ionization state of the interplanetary plasma. *J. Geophys. Res. (1896-1977)* 73, 5485–5493. doi:10.1029/JA073i017p05485

Jian, L., Russell, C., and Luhmann, J. (2011). Comparing solar minimum 23/24 with historical solar wind records at 1 au. *Sol. Phys.* 274, 321–344. doi:10.1007/s11207-011-9737-2

Ko, Y., Fisk, L., Geiss, J., Gloeckler, G., and Guhathakurta, M. (1997). An empirical study of the electron temperature and heavy ion velocities in the south polar coronal hole. *Sol. Phys.* 171, 345–361. doi:10.1023/A:1004943213433

Laming, J. (2015). The fip and inverse fip effects in solar and stellar coronae. *Living Rev. Sol. Phys.* 12, 2. doi:10.1007/lrsp-2015-2

Laming, J. M., Vourlidas, A., Korendyke, C., Chua, D., Cranmer, S. R., Ko, Y.-K., et al. (2019). Element abundances: a new diagnostic for the solar wind. *Astrophysical J.* 879, 124. doi:10.3847/1538-4357/ab23f1

Landi, E., Alexander, R. L., Gruesbeck, J. R., Gilbert, J. A., Lepri, S. T., Manchester, W. B., et al. (2012a). Carbon ionization stages as a diagnostic of the solar wind. *Astrophysical J.* 744, 100. doi:10.1088/0004-637X/744/2/100

Landi, E., Gruesbeck, J. R., Lepri, S. T., Zurbuchen, T. H., and Fisk, L. A. (2012b). Charge state evolution in the solar wind. ii. plasma charge state composition in the inner corona and accelerating fast solar wind. *Astrophysical J.* 761, 48. doi:10.1088/0004-637X/761/1/48

Lepri, S. T., and Zurbuchen, T. H. (2004). Iron charge state distributions as an indicator of hot icmes: possible sources and temporal and spatial variations during solar maximum. *J. Geophys. Res. Space Phys.* 109. doi:10.1029/2003JA009954

Livi, S., Lepri, S. T., Raines, J. M., Dewey, R. M., Galvin, A., Louarn, P., et al. (2023). First results from the solar orbiter heavy ion sensor. *A&* 676, A36. doi:10.1051/0004-6361/202346304

Lundin, R., and Guglielmi, A. (2006). Ponderomotive forces in cosmos. *Space Sci. Rev.* 127, 1–116. doi:10.1007/s11214-006-8314-8

McComas, D., Bame, S., Barker, P., Feldman, W., Phillips, J., Riley, P., et al. (1998). Solar wind electron proton alpha monitor (swepam) for the advanced composition explorer. *Space Sci. Rev.* 86, 563–612. doi:10.1023/A:1005040232597

Müller, D., St. Cyr, O. C., Zouganelis, I., Gilbert, H. R., Marsden, R., Nieves-Chinchilla, T., et al. (2020). The solar orbiter mission - science overview. *A&* 642, A1. doi:10.1051/0004-6361/202038467

Owen, C. J., Bruno, R., Livi, S., Louarn, P., Al Janabi, K., Allegrini, F., et al. (2020). The solar orbiter solar wind analyser (swa) suite. *A&A* 642, A16. doi:10.1051/0004-6361/201937259

Raines, J., Lepri, S., Zurbuchen, T., Gloeckler, G., and Fisk, L. (2005). "Heavy ions in the solar wind: a new dataset from ACE," in *Connecting Sun and heliosphere: Proceedings of the conference solar wind 11 - SOHO 16* (Netherlands: ESA Publications Division), 539.

Richardson, I., and Cane, H. (2010). Near-earth interplanetary coronal mass ejections during solar cycle 23 (1996–2009): Catalog and summary of properties. *Sol. Phys.* 264, 189–237. doi:10.1007/s11207-010-9568-6

Richardson, I. G., and Cane, H. V. (2004). Identification of interplanetary coronal mass ejections at 1 au using multiple solar wind plasma composition anomalies. *J. Geophys. Res. Space Phys.* 109. doi:10.1029/2004JA010598

Rivera, Y., Higginson, A., Lepri, S., Viall, N., Alterman, B., Landi, E., et al. (2022). Deciphering the birth region, formation, and evolution of ambient and transient solar wind using heavy ion observations. *Front. Astron. Space Sci.* 9. doi:10.3389/fspas.2022.1056347

Rivera, Y. J., Landi, E., Lepri, S. T., and Gilbert, J. A. (2019). Empirical modeling of cme evolution constrained to ace/swics charge state distributions. *Astrophysical J.* 874, 164. doi:10.3847/1538-4357/ab0e11

Shearer, P., von Steiger, R., Raines, J. M., Lepri, S. T., Thomas, J. W., Gilbert, J. A., et al. (2014). The solar wind neon abundance observed with ace/swics and ulysses/swics. *Astrophysical J.* 789, 60. doi:10.1088/0004-637X/789/1/60

SIDC-Team, World data center for the sunspot index, and royal observatory of Belgium (1981). Accessed June 11, 2024.

Stakhiv, M., Landi, E., Lepri, S. T., Oran, R., and Zurbuchen, T. H. (2015). On the origin of mid-latitude fast wind: challenging the two-state solar wind paradigm. *Astrophysical J.* 801, 100. doi:10.1088/0004-637X/801/2/100

Stakhiv, M., Lepri, S. T., Landi, E., Tracy, P., and Zurbuchen, T. H. (2016). On solar wind origin and acceleration: measurements from ace. *Astrophysical J.* 829, 117. doi:10.3847/0004-637X/829/2/117

von Steiger, R., Schwadron, N. A., Fisk, L. A., Geiss, J., Gloeckler, G., Hefti, S., et al. (2000). Composition of quasi-stationary solar wind flows from ulysses/solar wind ion composition spectrometer. *J. Geophys. Res. Space Phys.* 105, 27217–27238. doi:10.1029/1999JA000358

Zhao, L., and Landi, E. (2014). Polar and equatorial coronal hole winds at solar minima: from the heliosphere to the inner corona. *Astrophysical J.* 781, 110. doi:10.1088/0004-637X/781/2/110

Zhao, L., Landi, E., Lepri, S., Gilbert, J., Zurbuchen, T., Fisk, L., et al. (2017). On the relation between the *in situ* properties and the coronal sources of the solar wind. *Astrophysical J.* 846, 135. doi:10.3847/1538-4357/aa850c

Zhao, L., Landi, E., Zurbuchen, T., Fisk, L., and Lepri, S. (2014). The evolution of 1 au equatorial solar wind and its association with the morphology of the heliospheric current sheet from solar cycles 23 to 24. *Astrophysical J.* 793, 44. doi:10.1088/0004-637X/793/1/44

Zhao, L., Zurbuchen, T., and Fisk, L. (2009). Global distribution of the solar wind during solar cycle 23: ace observations. *Astrophysical J.* 36. doi:10.1029/2009GL039181

Zurbuchen, T. H., Fisk, L. A., Gloeckler, G., and von Steiger, R. (2002). The solar wind composition throughout the solar cycle: a continuum of dynamic states. *Geophys. Res. Lett.* 29, 66–1–66–4. doi:10.1029/2001GL013946

Zurbuchen, T. H., Weberg, M., von Steiger, R., Mewaldt, R. A., Lepri, S. T., and Antiochos, S. K. (2016). Composition of coronal mass ejections. *Astrophysical J.* 826, 10. doi:10.3847/0004-637X/826/1/10